Toward Controllable Quantum Transports and Novel Magnetic States in Eu1−xSrxMnSb2

Qiang Zhang (zhangq6@ornl.gov)
ORNL https://orcid.org/0000-0003-0389-7039

Jinyu Liu
Tulane University

Huibo Cao
Oak Ridge National Laboratory https://orcid.org/0000-0002-5970-4980

Adam Phelan
Department of Physics and Astronomy, Louisiana State University

John DiTusa
Department of Physics and Astronomy, Louisiana State University

David Tennant
Oak Ridge National Laboratory https://orcid.org/0000-0002-9575-3368

Zhiqiang Mao
Tulane University and Pennsylvania State University

Article

Keywords: Magnetic semimetal, novel spintronic device, topological semimetallic behavior, distinct collinear antiferromagnetic, fermion

Posted Date: September 17th, 2021

DOI: https://doi.org/10.21203/rs.3.rs-799050/v1

Toward controllable quantum transports and novel magnetic states in $Eu_{1-x}Sr_xMnSb_2$

Qiang Zhang[1,2+], Jinyu Liu[3+], Huibo Cao[1], Adam Phelan[2], J. F. DiTusa[2] D. Alan Tennant[1,4,5], & Zhiqiang Mao[3,6]

[1]*Neutron Scattering Division, Oak Ridge National Laboratory, Oak Ridge, TN 37831, USA*

[2]*Department of Physics and Astronomy, Louisiana State University, Baton Rouge, LA 70803, USA*

[3]*Department of Physics and Engineering Physics, Tulane University, New Orleans, Louisiana 70118, United States, USA*

[4]*Shull Wollan Center, Oak Ridge National Laboratory, Oak Ridge, Tennessee 37831, USA*

[5]*Quantum Science Center, Oak Ridge, Tennessee 37831, USA*

[6]*Department of Physics, Pennsylvania State University, University Park, PA 16802, USA*

August 9, 2021

Magnetic semimetals carry a great promise for potential applications in novel spintronic devices. Nevertheless, it is a challenging topic to realize the tunable topological states by the magnetism in a controllable way. Here, we report novel magnetic states and a tunability of the topological semimetallic states via controlling the Eu spin reorientation in $Eu_{1-x}Sr_xMnSb_2$. Increasing the Sr concentration in this system induces a surprising reorientation of noncollinear Eu spins to the Mn moment's direction and an appearance of topological semimetallic behavior. The Eu spin reorientations to distinct collinear antifer-

romagnetic orders are also driven by the temperature/magnetic field, which are coupled to transport properties of the relativistic fermions generated the 2D Sb layers. These results suggest nonmagnetic element doping to the rare-earth element site may be an effective strategy to generate topological electronic states and new magnetic states in layered compounds involving spatially separated rare-earth and transition metal layers.

1 Introduction

Dirac/Weyl semimetals have attracted intense research interest due to their exotic quantum phenomena as well as promising applications in the next generation, more energy efficient electronic devices.[1–3] Magnetic Dirac/Weyl semimetals are especially attractive since the coupling of Dirac/Weyl fermions to the additional spin degree of freedom may open up a new avenue to tune and control resulting quantum transport properties.[4–6] To date, a couple of magnetic semimetals have been reported and most of the them were discovered in stoichiometric compounds, such as $SrMnBi_2$[7], Mn_3Sn[8], RAlGe(R = rare earth)[9], $Co_3Sn_2S_2$[10], Co_2MnGa[11,12], etc. Finding a strategy to control a topological state by tuning magnetism is highly desired and requires clear understanding of the interplay between the magnetism and the topological electronic state. This goal can be achieved by investigating the coupling between the structure, magnetic and electronic phase diagrams in tunable magnetic topological materials.

A large family of ternary $AMnCh_2$ "112" compounds (A =alkali earth/rare earth elements, Ch = Bi or Sb)[6,7,13–15] are particularly interesting since a few of them have been reported to be magnetic Dirac semimetals where the Bi or Sb layers host relativistic fermions. $AMnCh_2$ (A=Ce,

Pr, Nd, Eu, Sm; C=Bi or Sb)[15–17] possesses two magnetic sub-lattices, formed by the magnetic moments of rare-earth A and Mn respectively, in contrast with other compounds showing only Mn magnetic lattice in this family. The conducting Bi/Sb layers and the insulating magnetic Mn-Bi(Sb) and Eu layers are spatially separated, which makes them good candidates to explore the possible interplay between Dirac fermions and magnetism. For $EuMnBi_2$, both Eu and Mn moments point to the out-of-plane direction and generate two AFM lattices in the ground state [15]. Previous studies have also shown that when the Eu AFM order undergoes a spin-flop transition in a moderate field range, the interlayer conduction is strongly suppressed, thus resulting in a stacked quantum Hall effect [15]. Interestingly, $EuMnSb_2$ exhibits distinct properties from $EuMnBi_2$ and conflicting results have been reported [16–18]. The magneto-transport properties reported by Yi et al. [16] are not indicative of a Dirac semimetallic state, while Soh et al. [17] observed linear band dispersion near the Fermi level in the ARPES measurements of $EuMnSb_2$ and claimed it may be a Dirac semimetal. Moreover, the magnetic structure of $EuMnSb_2$ is also thought to be distinct from that of $EuMnBi_2$, with controversial reports on Eu and Mn moments being perpendicular [17] or canted to each other [18]. It is therefore important to resolve the controversial magnetic and physical properties of $EuMnSb_2$ and to explore whether $EuMnSb_2$ and its derivatives could host Dirac fermions. Additionally, it is known that in many layered compounds involving spatially separated rare-earth and manganese layers such as RMnAsO (R=Nd or Ce) [19,20] and RMnSbO (R=Pr or Ce) [21,22], the moment of rare-earth element ordered at low temperatures usually drives a Mn spin reorientation to its moment direction. Given there are two magnetic sublattices of Eu and Mn with an expected $4f$-$3d$ coupling between them in $EuMnSb_2$, the chemical substitution of Eu by nonmagnetic element may

achieve interesting magnetic states via tuning the magnetic interactions, which may control the transport and magneto-transport properties.

In this article, we report comprehensive studies on a tunable Dirac semimetal system $Eu_{1-x}Sr_xMnSb_2$, which exhibits a variety of novel magnetic states tunable by the Eu concentration, temperature and magnetic field. The evolution of magnetic states of this system is found to be coupled to quantum transport properties of Dirac fermions. Through single crystal X-ray diffraction, neutron scattering, magnetic and high-field transport measurements, we have established a rich phase diagram of crystal structure, magnetism and electronic properties of $Eu_{1-x}Sr_xMnSb_2$. The increase of Sr concentration in $Eu_{1-x}Sr_xMnSb_2$ induces not only a lattice symmetry breaking, a surprising Eu spin reorientation to the Mn moment direction, but also topological semimetallic states for $x \geq 0.5$. Further, the quantum transport properties can also be tuned by the different Eu spin reorientations to collinear AFM orders induced by the temperature and external magnetic field. The in-plane and out-of-plane components of the canted Eu magnetic order are found to influence the intralayer and interlayer conductivity of Dirac fermions generated by the 2D Sb layers, respectively. These results establish a new unique material platform for exploring the Dirac band tuning by magnetism.

2 Materials and Methods

Crystal growth The $Eu_{1-x}Sr_xMnSb_2$ (x=0, 0.2, 0.5, 0.8) single crystals were grown using a self-flux method. The starting materials with a stoichiometric mixture of Eu/Sr, Mn and Sb elements were put into a small alumina crucible and sealed in a quartz tube in an argon gas atmosphere. The

tube was heated to 1050 ^{o}C for 2 days, followed by a subsequent cooling to 650 ^{o}C at a rate of 2 ^{o}C/h. Plate-like single crystals were obtained.

Single-crystal x-ray and neutron diffraction measurements and neutron data analysis A crystal of x=0 was mounted onto a glass fibers using epoxy, which was in turn then mounted onto the goniometer of a Nonius KappaCCD diffractometer equipped with Mo Kα radiation (λ = 0.71073 $\mathring{A}$). After the data collection and subsequent data reduction, SIR97 was employed to give a starting model, SHELXL97 was used to refine the structural model, and the data were corrected using extinction coefficients and weighting schemes during the final stages of refinement.[23,24] To investigate the crystal and magnetic structures, neutron diffraction measurements were conducted at the four circle neutron diffractometer (FCD), located at the High Flux Isotope Reactor, Oak Ridge National Laboratory. To further distinguish between tetragonal and orthorhombic structures for x=0, neutrons with a monochromatic wavelength of 1.003 Å without λ/2 contamination are used via the silicon monochromator from (bent Si-331) [25]. For other $Eu_{1-x}Sr_xMnSb_2$ (x= 0.2, 0.5, 0.8) crystals, we employed the neutrons with a wavelength of 1.542 Å involving 1.4 % $\lambda/2$ contamination from the Si-220 monochromator using its high resolution mode (bending 150) [25]. The crystal and magnetic structures were investigated in different temperature windows. The order parameter of a few important nuclear and magnetic peaks was measured. Data were recorded over a temperature range of $4 < T < 340$ K using a closed-cycle refrigerator available at the FCD. Due to the involvement of the high absorbing Europium in the $Eu_{1-x}Sr_xMnSb_2$ crystals, a proper neutron absorption corrections on the integrated intensities of the nuclear/magnetic peaks is indispensable. The dimensions of the faces for each crystal were measured and a Face Index

Absorption Correction on integrated intensities was conducted carefully using WinGX package [26]. The SARAH representational analysis program [27] and Bilbao crystallographic server [28] were used to derive the symmetry-allowed magnetic structures and magnetic space groups. The full data sets at different temperatures were analyzed using the refinement program FullProf suite [29] to obtain the structure and magnetic structures.

Magnetization, and magneto-transport measurements The temperature and field dependence of the magnetization were measured in a superconducting quantum interference device magnetometer (Quantum Design) in magnetic fields up to 7 T. The transport measurements at zero magnetic field were performed with a four-probe method using Physical Property Measurement Systems (PPMS). The high-field magneto-transport properties were measured in the 31 T resistivity magnets at the National High Magnetic Field Laboratory (NHMFL) in Tallahassee. The magnetic fields were applied parallel to out-of-plane direction to study the in-plane and out-of-plane magnetoresistance. The ρ_{in} samples were made into hall bar shape and the ρ_{zz} samples were in Corbino disk geometry. Berry phase was extracted from the Landau fan diagram. The integer Landau levels are assigned to the magnetic field positions of resistivity minima in SdH oscillations, which correspond to the minimal density of state.

3 Results and Discussion

Crystal structures Both single crystal x-ray and neutron diffraction reveal that the parent compound $EuMnSb_2$ crystallizes in a tetragonal structure with space group $P4/nmm$ (Fig. 1(b) and

S1(e)) and nonstoichiometric composition $EuMn_{0.95}Sb_2$. The structural parameters of $EuMn_{0.95}Sb_2$ obtained from the single crystal x-ray diffraction refinement at 293 K are summarized in Table SI and SII. Note that the structure of $EuMn_{0.95}Sb_2$ is similar to that of $CaMnBi_2$[30], but different from the $I4/mmm$ in tetragonal structure of $EuMn_{0.95}Bi_2$[15] and the previously reported orthorhombic structure of $EuMnSb_2$[16–18]. The Sr-doped $Eu_{1-x}Sr_xMnSb_2$ (x=0.2, 0.5 and 0.8), however, show a clear lattice distortion and crystallize in the orthorhombic structure with the space group $Pnma$, with a doubled unit cell along the out-of-plane direction (Fig. 1(c-d) and S1(f)), similar to $SrMnSb_2$[6]. The structural parameters of $Eu_{1-x}Sr_xMnSb_2$ (x=0, 0.2, 0.5 and 0.8) at 5 K obtained from the fits to neutron diffraction data are summarized in Table I. It can be seen that the Sr doping induces a slight decrease of out-of-plane lattice constant and an increase of in-plane lattice constants. More details of the determination of crystal structures of all the $Eu_{1-x}Sr_xMnSb_2$ compounds can be found in Supplemental Information.

Determination of magnetic structures In general, determining the complicated magnetic structures in Eu-containing compounds is hard due to strong neutron absorption of europium. A proper neutron absorption correction on the neutron diffraction data is critical. We employed single crystal neutron diffraction to solve the complicated magnetic structures of $Eu_{1-x}Sr_xMnSb_2$ below $\approx$ 340 K. The refined moments, Mn-Eu canting angle and reliability factors of the refinements on the neutron data after neutron absorption correction are summarized in Table II (see more details in supplemental information).

Figure 2 (a-d) show the temperature dependences of a few representative nuclear and/or

magnetic reflections of $Eu_{1-x}Sr_xMnSb_2$. For the x=0 parent compound, the presence of the pure magnetic peak at $(100)_{\rm T}$ below $T_1 \approx 330$ K indicates one magnetic transition. The absence of an anomaly at T_1 in susceptibility measurements (see Fig. 3(a)) may be ascribed to the possible strong spin fluctuations above T_1 that tend to smear out any anomaly in the susceptibility as in other Mn-based compounds [6,19,21]. For $T < T_1$, a C-type AFM order of Mn spins ($AFM_{\rm Mn}$) with the propagation vector $\mathbf{k} = (0,0,0)_{\rm T}$ and moment along the c_T axis is determined without Eu ordering, as illustrated in the left panel of Fig. 1 (b). Upon cooling below $T_2 \approx 22$ K, there is an increase of magnetic peak intensities such as $(100)_{\rm T}$ and $(101)_{\rm T}$ with $\mathbf{k} = (0,0,0)_{\rm T}$ and simultaneously, new magnetic reflections with a propagation vector $\mathbf{k} = (0,0,1/2)_{\rm T}$ from the Eu sublattice appear.

Interestingly, we observed strong magnetic peaks $(0,0,L/2)_{\rm T}$ (L= odd number) below T_2 (see inset of Fig. 2(a)). This excludes the possibility of Eu moments pointing in the out-of-plane axis seen in $EuMnBi_2$[15,31]. The determined magnetic structure for $T < T_2$ denoted by $AFM_{\rm Mn,Eu,\perp}$ is shown in the right panel of Fig. 1 (b). Whereas Mn preserves a C-type AFM order with an increased moment due to Eu-Mn coupling along the $c_{\rm T}$ axis, the "+ + - -" Eu spin ordering with moment along the $a_{\rm T}$ axis breaks magnetic symmetry along the $c_{\rm T}$ axis and leads to observed magnetic reflections with $\mathbf{k} = (0,0,1/2)_{\rm T}$. Such a magnetic structure is consistent with the susceptibility measurements where χ_c increases slightly and χ_{ab} decreases rapidly for $T < T_2$, suggesting an AFM moment oriented along the $a_{\rm T}b_{\rm T}$ plane. Note that the magnetic structure determined here is different from the "+-+-" A-type Eu order proposed on the basis of diffraction experiments on a polycrystalline sample $EuMnSb_2$ for which no $\mathbf{k} = (0,0,1/2)_{\rm T}$ magnetic peaks were observed below T_2. The Eu moment's canting proposed in *Ref.* 12 is not found in our crystal for $T < T_2$ in

our crystal (see Supplemental Information for detailed discussion).

In the x=0.2 sample, we observed pure magnetic peaks $(010)_{\rm O}$ and $(001)_{\rm O}$ in the orthorhombic structure as shown in Fig. 2(b), corresponding to $(100)_{\rm T}$ in the tetragonal notation, below $T_1 \approx 330$ K and determined a similar C-type AFM order ($\rm AFM_{Mn}$) with $\mathbf{k} = (0,0,0)_{\rm O}$ as shown in the left panel in Fig. 1(c). Upon cooling below $T_2 \approx 21$ K, new magnetic peaks indexed by (H,K,L) (H=odd integers), for instance $(700)_{\rm O}$, corresponding to $(0\ 0\ 3.5)_{\rm T}$, are observed (see inset of Fig. 2 (b)). All the magnetic peaks can be described by the AFM order at $\mathbf{k} = (0,0,0)_{\rm O}$ in the orthorhombic notation due to doubled unit cell as compared to x=0. Within the temperature range of $T_3 < T < T_2$, we found a canted and noncollinear Eu spin order confined within ac plane with a "+ + - -' component along $c_{\rm O}$ axis and a "+ - + -" component along the $a_{\rm O}$ axis, coexisting with the C-type Mn AFM order with the moments along the $a_{\rm O}$ axis (denoted by $\rm AFM_{Mn,Eu,C1}$, the middle panel in Fig. 1(c)). This is consistent with the susceptibility measurement shown in Fig. 3(b) where both χ_a and χ_{bc} decrease below T_2, implying that Eu spins may form a canted AFM order. Note that such a canted Eu order is not applicable in the corresponding $T < T_2$ temperature region of the x=0 parent compound. At 10 K, the canting angle between Mn and Eu is 41(9) $^{\rm o}$. The susceptibility measurements show that χ_a increases but χ_{bc} decreases anomalously below $T_3 \approx 7$ K, indicative of another magnetic transition. Interestingly, there is a decrease of the $(300)_{\rm O}$ peak intensity, with a concurrent increase of intensity of the nuclear peak $(600)_{\rm O}$ for $T < T_3$. This strongly indicates a Eu spin-reorientation transition to a Eu spin order without a magnetic symmetry breaking along the $a_{\rm O}$ axis. While the C-type Mn order is unchanged, a canted and collinear magnetic structure with A-type "+ - + -" Eu spin order along both $a_{\rm O}$ and $c_{\rm O}$ axes ($\rm AFM_{Mn,Eu,C2}$)

occurs with a Mn-Eu canting angle of 40(7)^{o} at 4 K, as shown in the right panel of Fig. 1(c). At 4 K, the Mn and Eu moments are found to be 3.75(45) and 5.26(50) μ_B, respectively, indicative of Mn^{2+} ($S = 5/2$) and Eu^{2+} ($S = 7/2$).

When x is increased to 0.5 or 0.8, the Eu lattice exhibits only a single AFM transition as revealed from susceptibility measurements shown in Fig. 3(c), with $T_2 \approx 17$ K for x=0.5 and 8 K for x=0.8. For the x=0.5 sample, both the $(010)_{\rm O}$ and $(001)_{\rm O}$ magnetic peaks appear below T_1. Upon cooling below $T_2 \approx 15$ K, the $(010)_{\rm O}$ peak intensity further increases while there is no obvious change in the $(001)_{\rm O}$ (see Fig. 2(c) and Fig. S5(a-b)). Furthermore, there is an increase of peak intensity $(300)_{\rm O}$ due to magnetic contribution but no obvious change in peak intensities of $(200)_{\rm O}$ or $(600)_{\rm O}$. These features are similar to those in x=0.2. We indeed obtained the similar magnetic structures in the x=0.5 sample, as shown in the left panel ($AFM_{\rm Mn}$) and middle one ($AFM_{\rm Mn,Eu,C1}$) in Fig. 1 (c) for $T_2 < T < T_1$ and $T_3 < T < T_2$, respectively. Note that the canting angle between Eu and Mn moments decreases to $\approx 24^{o}$ at 5 K.

As x increases to 0.8, the Mn magnetic transition occurs at a temperature $T_1 \approx 330$ K as identified from the intensity of $(010)_{\rm O}$ and a C-type Mn order $AFM_{\rm Mn}$ is determined (see the left panel of Fig. 1(d)). Another increase of $(010)_{\rm O}$ is found below $T_2 \approx 7$ K. There is no appearance of magnetic scattering at the $(300)_{\rm O}$ and $(200)_{\rm O}$ or $(600)_{\rm O}$ Bragg positions below T_2 (see Fig. 1 (d) and Fig. S5(c-d) in SI), indicating that Eu moments may point to the $a_{\rm O}$ axis. We found a coexistence of Mn C-type AFM order with the "+ - + -" Eu order with oriented moment along the same the $a_{\rm O}$ axis as the Mn moment ($AFM_{\rm Mn,Eu,\|}$, see the right panel of Fig. 1 (d)), consistent

with susceptibility measurements. As shown in Fig. 3(c), χ_{bc} keeps increasing but χ_a decreases rapidly upon cooling below 8 K, showing the opposite behavior to x=0. This indicates that the Eu moment mainly points to out-of-plane $a_{\rm O}$ direction in x=0.8.

Electronic transport properties Next, we present the evolution of electronic transport properties with the Sr doping in $Eu_{1-x}Sr_xMnSb_2$. As shown in Fig. 3(d-f), both in-plane (ρ_{in}) and out-of-plane resistivity (ρ_{out}) exhibit metallic transport properties. At 2 K, the ρ_{out}/ρ_{in} reaches 128, 198 and 322, for x=0, x=0.2 and x=0.8, respectively. Such a rapid increase of electronic anisotropy indicates that Sr doping reinforces the quasi-2D electronic structure. In the x=0 sample, the slope of ρ_{out} and ρ_{in} decreases below T_2, indicative of the coupling between the emergence of Eu order and transport properties, suggesting that the in-plane Eu "+ + - - " order leads to suppressed metalicity. The metallic behavior in our $EuMn_{0.95}Sb_2$ sample is different from the insulating behavior observed in the Sn- or Mn-doped nonstoichiometric samples[16,18]. This indicates that the chemical doping on Sb or Mn sites induces a metal-insulator transition, which is distinct from the effect of the Sr substitution for Eu.

However, the x=0.2 sample exhibits distinct transport behavior as compared to x=0 sample. We observed a rapid decrease in ρ_{out} and a slight increase in ρ_{in} below T_2, suggesting that the Eu canting to the $a_{\rm O}$ axis with the Eu "+ - + - " component significantly increases the interlayer conductivity along the $a_{\rm O}$ direction between Sb layers but suppresses the intralayer conductivity on the $b_{\rm O}c_{\rm O}$ plane, contrasted with the effect of of the sole in-plane Eu order on the transport properties as described above. Below T_3, there is no obvious change in the out-of-plane resistivity,

but an anomalous decrease of the in-plane resistivity is observed. This can be well interpreted from the SR of Eu from noncollinear to collinear order. Below T_3, the out-of-plane Eu order is kept to be "+ - + - ", which is not expected to influence the interlayer conductivity. In contrast, the switch of the in-plane component from "+ + - - " to "+ - + -" induces the anomalous increase in the intralayer conductivity.

As for x=0.8, the Eu ordering does not influence the resistivity obviously below T_2, which can be ascribed to the small portion of Eu occupancy ($\approx 20\ \%$). Thus, our results reveal an intimate coupling between the Eu magnetic order and transport properties in $Eu_{1-x}Sr_xMnSb_2$.

Nontrivial Berry phases Figure 4 (a-d) shows both in-plane and out-of-plane magnetoresistance ($MR = [\rho(B) - \rho(0)]/\rho(0)$) under high magnetic fields applied along the out-of-plane direction. For x=0, the $\Delta\rho_{out}/\rho_{out}$ is negative, whereas the in-plane $\Delta\rho_{in}/\rho_{in}$ is positive. The magnitudes for both $\Delta\rho_{out}/\rho_{out}$ and $\Delta\rho_{in}/\rho_{in}$ are small, and no strong Shubnikov-de Haas (SdH) oscillations are observed. For x=0.2, weak SdH oscillations are observed in both $\Delta\rho_{out}/\rho_{out}$ and $\Delta\rho_{in}/\rho_{in}$. As the field increases, there is a sign reversal in $\Delta\rho_{in}/\rho_{in}$, whereas the $\Delta\rho_{out}/\rho_{out}$ remains positive. Remarkably, at 1.8 K that is below T_3, a large jump in $\Delta\rho_{out}/\rho_{out}$ up to $\approx 4500\ \%$ occurs above $\mu_0 H_t \approx 18$ T, followed by a rapid decrease above ≈ 27 T. The dramatic changes in $\Delta\rho_{out}/\rho_{out}$ are ascribed to a field-induced metamagnetic transition. Since this phenomenon does not occur in the $T > T_2$ temperature regime (e.g. 50 K), the field-induced magnetic transition should not originate from the Mn magnetic sublattice, but be related to the Eu magnetic sublattice, indicative of a vital role that the Eu magnetic order plays in the magneto-transport properties. The most possible origin

of the enhanced $\Delta\rho_{out}/\rho_{out}$ above $\mu_0 H_t$ is the field-induced Eu SR transition from canted moment direction in $a_{\rm O}c_{\rm O}$ plane to the $c_{\rm O}$ axis while the A-type "+ - + -" Eu order remains, thus yielding a strong suppression of interlayer conductivity, as illustrated in the inset of Fig. 4(b). Note that this is different from the filed-induced spin flop transition of the "+ + - -" Eu order from out-of-plane $c_{\rm O}$ axis to in-plane direction in $EuMnBi_2$[15]. Above $\mu_0 H_s \approx 27$ T, the rapid decrease of $\Delta\rho_{out}/\rho_{out}$ results from the full polarization of Eu spins to external filed direction, i.e., $a_{\rm O}$ axis, similar to the scenario seen in $EuMnBi_2$[15].

The increase of the Sr doping level enhances SdH oscillations significantly in both $\Delta\rho_{out}/\rho_{out}$ and $\Delta\rho_{in}/\rho_{in}$ for x=0.5 and 0.8, with much higher oscillation amplitudes at high magnetic fields. $\Delta\rho_{out}/\rho_{out}$ reaches $\approx 18000\%$ at 31.5 T for x=0.8. We further analyzed the Berry phase (BP) ϕ_B accumulated along cyclotron orbits and are able to extract ϕ_B for x=0.5 and 0.8. From the linear fit of the Landau level fan diagram based on the oscillatory resistivity ρ_{in}, we obtained intercept n_0 of 0.38 and 0.44 for x=0.5 and x=0.8, respectively, as shown in the insets of Fig. 4 (c-d). The corresponding Berry phases $2\pi\times$ n_0 are 0.76 π for x=0.5 and 0.88 π for x=0.8. The fits to LL fan diagram based on the oscillatory resistivity ρ_{out} for x=0.8 yield intercept n_0 of 0.57, with a corresponding Berry phases of 1.14 π. All of them are close to a nontrivial π Berry phase for a quasi 2D system. The non-trivial Berry phase provides the evidences that x=0.5 and 0.8 harbor relativistic Dirac fermions. Our results clearly show that the substitution of Eu by nonmagnetic Sr induces Dirac semimetallic behavior, which is closely associated with the controllable Eu magnetic order.

Unlike the x=0.2 sample, the x=0.5 and 0.8 samples do not show large jumps in $\Delta\rho_{out}/\rho_{out}$

in field up to 31 T. This indicates the absence of the field-induced metamagnetic transitions in both compounds. So the non-trivial Berry phase may be intrinsic for x=0.5 and 0.8 compounds. In addition, as compared to $SrMnSb_2$ with only ordered Mn moment, the x=0.5 and 0.8 samples exhibit distinct Eu orders coexisting with Mn orders and the increase of Eu canting angle is accompanied with stronger quantum oscillations.

Composition phase diagram From the combination of single crystal x-ray diffraction, neutron diffraction, magnetization, and magneto-transport measurements, we are able to establish the structural, magnetic and electronic phase diagram, as shown in Fig. 1 (a). While the x=0 parent compound with Mn deficiency is tetragonal with space group $P4/nmm$, the Sr-doping induces an orthorhombic distortion. This is consistent with the previous reports on the orthorhombic structure in the doped nonstoichiometric samples[16,18]. It is worthwhile pointing out that our $EuMn_{0.95}Sb_2$ sample forms a magnetic structure with perpendicular Mn and Eu moments at the ground state and does not exhibit topological semimetallic behavior, both of which are distinct from the previous reports on the samples with different compositions[16–18]. The Sr substitution for Eu in $EuMnSb_2$ induces a slight decrease of T_1 but suppresses T_2 significantly. Furthermore, the increase of Sr concentration drives an unusual Eu SR from the in-plane to the out-of-plane direction and simultaneously induces the Dirac semimetallic behaviors. A higher Eu canting angle characterized by a smaller Eu-Mn angle is accompanied with the stronger quantum SdH oscillations. Our results show that the Eu spin canting can be driven by the chemical doping, which could interpret the observation of Eu canting in doped nonstoichiometric sample[18]. It is worthwhile pointing out that there is no another magnetic transition at T_3 observed in Ref. [18]. For our x=0.2 compound, the

2nd type of Eu SR from a noncollinear canted spin order to a collinear A-type canted spin order was found at lower temperature (denoted by $AFM_{Mn,Eu,C2}$ in Fig. 1(a)). Furthermore, the Eu order at the base temperature can be easily tuned by the external magnetic field to another type of SR, leading to a canted AFM state with the moments orientedto the possible c_O axis. The established phase diagram for $Eu_{1-x}Sr_xMnSb_2$ as well as the comparison with the previous reports we made above[16–18] indicate that the structure, magnetic order and electronic properties of $EuMnSb_2$ are easily perturbed by the chemical doping on any of the Eu, Mn and Sb sites, indicating lattice, spin and charge degrees of freedom are strongly coupled in this material. This could account for the conflicting results reported in the literatures[16–18] regarding the structure, magnetic and electronic transport properties of $EuMnSb_2$ and implies that the non-stoichiometry must be taken into account to understand the intrinsic crystal and magnetic structure, and magneto-transport properties of $EuMnSb_2$.

While the chemical doping on Sb or Mn sites[16,18] in nonstoichiometric samples induces the tetragonal-orthorhombic structural transition as in our $Eu_{1-x}Sr_xMnSb_2$ (x>0), such doping induces a metal-insulator transition yielding the insulating behavior. This indicates that the doping to the Sb or Mn sites may play a detrimental role in forming the semimetallic behavior in $EuMnSb_2$ derivatives. In contrast, our phase diagram clearly shows that the Sr doping to the Eu site is the driving force of the Dirac semimetallic behaviors in $Eu_{1-x}Sr_xMnSb_2$ as discussed below. First, the Sr doping to Eu site lowers the lattice symmetry and modifies structural parameters as summarized in Table I, which could in turn change the electronic band structure. Second, the different types of Eu spin reorientations driven by the Sr doping, temperature or magnetic field influence the

electronic transport and magneto-transport properties significantly, indicating the band structure is sensitively dependent on the magnetism of the Eu sub-lattice. As such, the phase diagram presented in Fig. 1 (a) offers an excellent opportunity to explore the intimate interplay between band relativistic effect and magnetism.

Origin of various Eu spin reorientations Finally, we turn to discuss the origins of the complicated magnetic structures, in particular the Sr-doping and temperature induced Eu SR transition in $Eu_{1-x}Sr_xMnSb_2$. A common SR of rare earth is that the rare-earth element drives Mn moment parallel to its moment direction once the rare earth spins are ordered with preferred in-plane orientation at low temperatures, as reported in several compounds such as RMnAsO (R=Nd or Ce) [19,20] and RMnSbO (R=Pr or Ce) [21,22]. However, the Sr doping in $Eu_{1-x}Sr_xMnSb_2$ generates a novel Eu SR with moment changing from the in-plane direction to the out-of-plane direction while Mn moment direction remains along the out-of-plane $a_{\rm O}$-axis.

The Mn^{2+} moment, which commonly displays very weak single-ion anisotropy as expected for the L=0 of Mn^{2+} ($S = 5/2$), favors orientation along the out-of-plane direction [19–21], i.e., the $c_{\rm T}$ axis in tetragonal structure or the $a_{\rm O}$ axis in orthorhombic structure, forming the C-type AFM order in $T_2 < T < T_1$ of $Eu_{1-x}Sr_xMnSb_2$. The in-plane checker-board-like AFM structure of the C-type order suggests that the NN interaction J_1 is dominant, whereas in-plane next-nearest-neighbor (NNN) interaction J_2 is very weak. In the context of $J_1 - J_2 - J_c$ model [32], we conclude that $J_1 > 0$, $J_2 < J_1/2$ and out-of-plane $J_c < 0$ with negligible spin frustration in Mn sublattice. Upon cooling to $T < T_2$, Eu-Eu coupling starts to come into play and induces Eu ordering with

preferred orientation of Eu^{2+} ($S = 7/2$) within in plane [33,34], either the $a_{\rm T}b_{\rm T}$ plane in tetragonal structure or the $b_{\rm O}c_{\rm O}$ plane in orthorhombic structure. Simultaneously, the Eu-Mn coupling also plays an important role by exerting an effective field, which has the tendency to influence the Mn/Eu moment directions. The increase of Sr concentration on Eu site weakens the Eu-Eu coupling and destabilizes the preferred orientation of the Eu spins. Thus, as x increases to 0.2, the effective field by Eu-Mn coupling tends to drive the Eu moment towards to the Mn moment direction. The competition of Eu-Eu and Eu-Mn couplings induces a spin frustration in Eu sublattice and leads to a canted Eu order with moment in ac plane stabilized in $T_3 < T < T_2$. The increase of Sr doping has a tendency to further drive Eu moment tilt towards the $a_{\rm O}$ axis due to weakened Eu-Eu coupling, as shown by a decreased Eu-Mn angle for x=0.5. As Sr doping increases to 0.8, the Eu-Mn coupling overwhelms the weak Eu-Eu coupling, which leads to a SR of Eu to the same moment direction as Mn moment. This could account for the unusual Eu SR induced by Sr doping. As the temperature decreases below T_3 for x=0.2, a temperature-induced SR transition occurs. This may be ascribed to another type of Eu-Eu coupling that comes into play below T_3. This retains "+ - + -" out-of-plane component but switches in-plane component from "+ + - -" to "+ - + -", leading to collinear A-type AFM order of Eu spins in $T < T_3$. Thus, the striking Eu spin reorientation driven by Sr doping and temperature indicates a strong Eu-Mn ($4f$-$3d$) couplings and results from their competitions to Eu-Eu couplings.

To summarize, we report the composition phase diagram of the crystal and magnetic structures, and electronic transport properties in $Eu_{1-x}Sr_xMnSb_2$ and the realization of the tunable topological semimetallic behavior via controlling various spin reorientations by chemical substi-

tution, temperature and/or external magnetic field. The structure, magnetic order and electronic properties of parent $EuMnSb_2$ are easily perturbed by the chemical doping and therefore, the non-stoichiometry must be taken into account to determine its intrinsic structure and physical properties. While we found that the nearly stoichiometric $EuMnSb_2$ is not a topological semimetal, a doping of nonmagnetic Sr on Eu site induces an intricate coupling between structure, various Eu spin reorientations and quantum transport properties, indicating that $Eu_{1-x}Sr_xMnSb_2$ is a wonderful platform for the study of the interplay between magnetism and topological properties of electronic band structure. The present study may be a stimulus to search for semimetallic states and interesting magnetic states in the large $AMnCh_2$ (A=rare-earth elements, such as Ce, Pr, Nd, Sm; Ch=Bi/Sb) family and other layered compounds involving spatially separated rare-earth and transition metal layers, by tuning the competition of $4f$-$3d$ and A-A magnetic couplings.

Acknowledgements Q.Z. J.L, A. P. and J. F.D. acknowledge support for the materials preparation and measurements of magnetization, transport and magneto-transport properties and neutron scatting from the US DOE under EPSCoR Grant No. DESC0012432 with additional support from the Louisiana board of regent. D.A.T. is sponsored by the DOE Office of Science, Laboratory Directed Research and Development program (LDRD) of Oak Ridge National Laboratory, managed by UT-Battelle, LLC for the U.S. Department of Energy. (Project ID 9566). Use of the high flux isotope reactor at Oak Ridge National Laboratory was supported by the U.S. Department of Energy, Office of Basic Energy Sciences, Scientific User Facilities Division.

Author contributions J.L. and Z.M. prepared and characterized the high-quality single crystals. A. P conducted single-crystal x-ray measurements and data analysis on x=0. Q.Z., H.C, J.D and D.A.T performed

the neutron experiments. J.L. and Z. M. analyzed magnetization and magneto-transport data. Q.Z. analyzed the neutron data and wrote the paper with the input from all the authors.

Competing Interests The authors declare that they have no competing financial interests.

Correspondence Correspondence and requests for materials should be addressed to Q.Z. (email: zhangq@ornl.gov).

1. Xu, S.-Y. *et al.* Discovery of a weyl fermion semimetal and topological fermi arcs. *Science* **349**, 613–617 (2015).

2. Lu, L. *et al.* Experimental observation of weyl points. *Science* **349**, 622–624 (2015).

3. Lv, B. Q. *et al.* Experimental discovery of weyl semimetal taas. *Phys. Rev. X* **5**, 031013 (2015).

4. Armitage, N. P., Mele, E. J. & Vishwanath, A. Weyl and Dirac semimetals in three-dimensional solids. *Rev. Mod. Phys.* **90** (2018).

5. Wan, X., Turner, A. M., Vishwanath, A. & Savrasov, S. Y. Topological semimetal and Fermi-arc surface states in the electronic structure of pyrochlore iridates. *Phys. Rev. B* **83** (2011).

6. Liu, J. Y. *et al.* A magnetic topological semimetal $\mathrm{Sr}_{1-y}\mathrm{Mn}_{1-z}\mathrm{Sb}_2$. *Nat. Mater.* **16**, 905 (2017).

7. Park, J. *et al.* Anisotropic dirac fermions in a bi square net of srmnbi_2. *Phys. Rev. Lett.* **107**, 126402 (2011).

8. Nakatsuji, S., Kiyohara, N. & Higo, T. Large anomalous Hall effect in a non-collinear antiferromagnet at room temperature. *NATURE* **527**, 212+ (2015).

9. Chang, G. *et al.* Magnetic and noncentrosymmetric weyl fermion semimetals in the $R\mathrm{AlGe}$ family of compounds ($R = \mathrm{rare\ earth}$). *Phys. Rev. B* **97**, 041104 (2018).

10. Liu, E. *et al.* Giant anomalous Hall effect in a ferromagnetic kagome-lattice semimetal. *Nat. Phys.* **14**, 1125 (2018).

11. Sakai, A. *et al.* Giant anomalous Nernst effect and quantum-critical scaling in a ferromagnetic semimetal. *NATURE PHYSICS* **14**, 1119+ (2018).

12. Belopolski, I. *et al.* Discovery of topological Weyl fermion lines and drumhead surface states in a room temperature magnet. *SCIENCE* **365**, 1278+ (2019).

13. Wollesen, P., Jeitschko, W., Brylak, M. & Dietrich, L. Ternary antimonides $\mathrm{LnM}_{1-x}\mathrm{Sb}_2$ with Ln=La−Nd, Sm, Gd, Tb and M=Mn, Co, Au, Zn, Cd . *J. Alloys. Compd.* **245** (1996).

14. Borisenko, S. *et al.* Time-reversal symmetry breaking type-II Weyl state in YbMnBi_2. *Nat. Commun.* **10** (2019).

15. Masuda, H. *et al.* Quantum Hall effect in a bulk antiferromagnet EuMnBi_2 with magnetically confined two-dimensional Dirac fermions. *Sci. Adv.* **2** (2016).

16. Yi, C. *et al.* Large negative magnetoresistance of a nearly dirac material: Layered antimonide EuMnSb_2. *Phys. Rev. B* **96**, 205103 (2017).

17. Soh, J.-R. *et al.* Magnetic and electronic structure of dirac semimetal candidate $\mathrm{EuMnSb_2}$. *Phys. Rev. B* **100**, 174406 (2019).

18. Gong, D. *et al.* Canted Eu magnetic structure in $\mathrm{EuMnSb_2}$. *Phys. Rev. B* **101**, 224422 (2020).

19. Zhang, Q., Tian, W., Peterson, S. G., Dennis, K. W. & Vaknin, D. Spin reorientation and ce-mn coupling in antiferromagnetic oxypnictide $\mathrm{CeMnAsO}$. *Phys. Rev. B* **91**, 064418 (2015).

20. Emery, N. *et al.* Variable temperature study of the crystal and magnetic structures of the giant magnetoresistant materials LMnAsO (L= $\mathrm{La, Nd}$). *Phys. Rev. B* **83**, 144429 (2011).

21. Zhang, Q. *et al.* Structure and magnetic properties of $\mathrm{LnMnSbO}$ ($\mathrm{Ln} = \mathrm{La}$ and Ce). *Phys. Rev. B* **93**, 094413 (2016).

22. Kimber, S. A. J. *et al.* Local moments and symmetry breaking in metallic $\mathrm{PrMnSbO}$. *Phys. Rev. B* **82**, 100412 (2010).

23. Altomare, A. *et al.* *SIR*97: a new tool for crystal structure determination and refinement. *J. Appl. Crystallogr* **32**, 115–119 (1999).

24. Sheldrick, G. M. A short history of *SHELX*. *Acta Crystallographica Section A* **64**, 112–122 (2008).

25. Chakoumakos, B. C. *et al.* Four-circle single-crystal neutron diffractometer at the High Flux Isotope Reactor. *J. Appl. Crystallogr* **44**, 655–658 (2011).

26. Farrugia, L. J. Wingx and ortep for windows: an update. *J. Appl. Crystallogr* **45**, 849–854 (2012).

27. Wills, A. A new protocol for the determination of magnetic structures using simulated annealing and representational analysis (sarah). *PHYSICA B* **276-278**, 680 – 681 (2000).

28. Perez-Mato, J. *et al.* Symmetry-based computational tools for magnetic crystallography. *Annu. Rev. Mater. Res.* **45**, 217–248 (2015).

29. Rodríguez-Carvajal, J. Recent advances in magnetic structure determination by neutron powder diffraction. *PHYSICA B* **192**, 55 – 69 (1993).

30. Zhang, A. *et al.* Interplay of Dirac electrons and magnetism in $CaMnB_2$ and $SrMnB_2$. *Nat. Commun.* **7** (2016).

31. Zhu, F. *et al.* Magnetic structures, spin-flop transition, and coupling of Eu and Mn magnetism in the dirac semimetal $\mathrm{EuMnBi_2}$. *Phys. Rev. Research* **2**, 043100 (2020).

32. Johnston, D. C. *et al.* Magnetic exchange interactions in $\mathrm{BaMn_2As_2}$: A case study of the J_1-J_2-J_c Heisenberg model. *Phys. Rev. B* **84**, 094445 (2011).

33. Herrero-Martin, J. *et al.* Magnetic structure of $\mathrm{EuFe_2As_2}$ as determined by resonant x-ray scattering. *Phys. Rev. B* **80**, 134411 (2009).

34. Xiao, Y. *et al.* Magnetic structure of $\mathrm{EuFe_2As_2}$ determined by single-crystal neutron diffraction. *Phys. Rev. B* **80**, 174424 (2009).

Figures and Tables

Fig. 1. (color online) (a). Composition phase diagram of $Eu_{1-x}Sr_xMnSb_2$ on the structural and magnetic transitions, Eu-Mn moment angle α and nontrivial Berry phase (BH) extracted from the fits to ρ_{in}. T_1, T_2, and T_3 label the magnetic transition temperatures. The distinct magnetic structures (AFM_{Mn}, $AFM_{Mn,Eu,\perp}$, $AFM_{Mn,Eu,C1}$, $AFM_{Mn,Eu,C2}$ and $AFM_{Mn,Eu,\parallel}$) are displayed in Fig. 1(b-d). $AFM_{Mn,Eu,\parallel}$ and $AFM_{Mn,Eu,\perp}$ indicate the parallel and perpendicular moments of Mn and Eu, respectively. $AFM_{Mn,Eu,C1}$ and $AFM_{Mn,Eu,C2}$ show the two distinct canted moments between Mn and Eu. The evolution of the violet color illustrates the gradual decrease of the Eu-Mn moment angles. A higher Eu canting angle of $(90^o - \alpha)$, i.e., a smaller α, is accompanied with the stronger quantum SdH oscillations. All the compounds exhibit metal-like transport properties as a function of temperature and they are also coupled to Eu order at T_2 and T_3. The non-trivial Berry phases indicative of Dirac semimetallic behaviors emerge with $x \geq$0.5. Magnetic structures determined from the fits to the neutron data for (b) x=0, (c) x=0.2 (all the panels) and 0.5 (only left and middle panels), and (d) x=0.8. The dashed rectangular shows the Mn-Eu-Eu-Mn block where the SR of Eu can be seen.

Fig. 2. (color online) Temperature dependence of intensities at the representative nuclear and/or magnetic peak positions for (a) x=0, (b) x=0.2, (c) x=0.5, and (d) 0.8. The insets show the comparison of the nuclear/magnetic peaks at different temperatures. The 2nd weak peak with smaller omega in the rocking curves for x=0 is due to the presence of another tetragonal domain rather than orthorhombic domain in the crystal. The very weak (300) peak in (d) results from the $\lambda/2$

contamination of neutrons. The vertical lines indicate the locations of the magnetic transition temperatures.

Fig. 3. (color online) Temperature dependence of susceptibility for (a) x=0 with magnetic field of 0.1 T parallel to out-of-plane $c_{\rm T}$ and in-plane $a_{\rm T}{\rm b}_{\rm T}$ directions, (b) x= 0.2, and (c) x=0.5 and 0.8, with field parallel to out-of-plane $a_{\rm O}$ and in-plane $b_{\rm O}{\rm c}_{\rm O}$ directions. Temperature dependence of resistivity at zero magnetic field for out-of-plane resistivity ρ_{out} and in-plane resistivity ρ_{in} for (d) x=0, (e) x=0.2 and (f) x=0.8.

Fig. 4. (color online) Field dependence of out-of-plane magnetoresistance $\Delta\rho_{out}/\rho_{out}$ and in-plane magnetoresistance $\Delta\rho_{in}/\rho_{in}$ for (a) x=0, (b) x=0.2, (c) x=0.5, and (d) x=0.8. The inset of Fig. (b) shows the field-induced metamagnetic transition in Eu-sublattice, i.e., Eu spin ordering in and $H < H_f$ and $H_f < H < H_s$. The inset of (c-d) shows the linear fit of the Landau level fan diagram based on the oscillatory resistivity ρ_{in} for x=0.5 and 0.8.

Table 1: Structural parameters of $Eu_{1-x}Sr_xMnSb_2$ with x=0, 0.2, 0.5, and 0.8 at 5 K obtained by the fits to the single crystal neutron diffraction data. For x=0, space group: $P4/nmm$. Atomic positions: Eu(2c): (0.25, 0.25, z), Mn(2a): (0.75, 0.25, 0), Sb_1(2b): (0.75, 0.25, 0.5), Sb_2(2c):(0.25, 0.25, z). For x>0 compounds: Space group: $Pnma$. Eu/Sr(4c): (x, 0.25, z), Mn(4c): (x, 0.25, z), Sb_1(4c):(x, 0.25, z), Sb_1(4c): (x, 0.25, z).

		x=0		x=0.2	x=0.5	x=0.8
lattice constants						
a		4.343(6)		22.348(3)	22.27(42)	22.28(41)
b		4.343(6)		4.347(5)	4.411(14)	4.412(14)
c		11.169(13)		4.383(4)	4.434(24)	4.438(28)
atom						
Eu	z	0.729(5)	x	0.113(4)	0.113(5)	0.112(4)
			z	0.781(5)	0.789(7)	0.806(3)
Mn			x	0.253(7)	0.249(4)	0.242(4)
			z	0.323(3)	0.279(7)	0.292(4)
Sb_1			x	0.0019(8)	0.0011(7)	0.0042(9)
			z	0.233(6)	0.264(4)	0.298(7)
Sb_2	z	0.156(7)	x	0.324(5)	0.325 (5)	0.324(6)
			z	0.829(5)	0.768(4)	0.818(5)
Reliable factors						
R_f		8.75		6.67	6.18	7.59
χ^2		0.28		0.28	1.21	0.83

Table 2: Refined magnetic moments, Mn-Eu angles and reliable factors of $Eu_{1-x}Sr_xMnSb_2$ with x=0, 0.2, 0.5, and 0.8 at different temperatures.

		x=0		x=0.2			x=0.5		x=0.8
	T (K)	170	5	60	10	4	50	5	5
Mn moments	$M_c(x=0)$	2.99(29)	4.63(21)						
	$M_a(x>0)$			3.70(46)	3.66(32)	3.75(45)	3.74(15)	3.76(17)	3.80(22)
Eu moments	M_a				4.08(34)	3.89(69)		4.84(55)	5.17(62)
	M_b								
	M_c		5.25(43)		3.52(34)	3.30(86)		2.23(29)	
	$\lvert M_{total}\rvert$		5.25(43)		5.38(34)	5.26(50)		5.32(50)	5.17(62)
Mn-Eu moment angle(^{o})			90(7)		41(9)	40(7)		24(8)	0
Reliable factors	$R_F(\mathbf{k}=(0,0,0))$	9.53	8.75	7.64	7.55	6.67	5.32	6.18	7.59
	$\chi_2(\mathbf{k}=(0,0,0))$	0.27	0.28	0.13	0.29	0.28	0.31	1.26	0.83
	$R_F(\mathbf{k}=(0,0,1/2))$		8.93						
	$\chi_2(\mathbf{k}=(0,0,1/2))$		0.26						

Figures

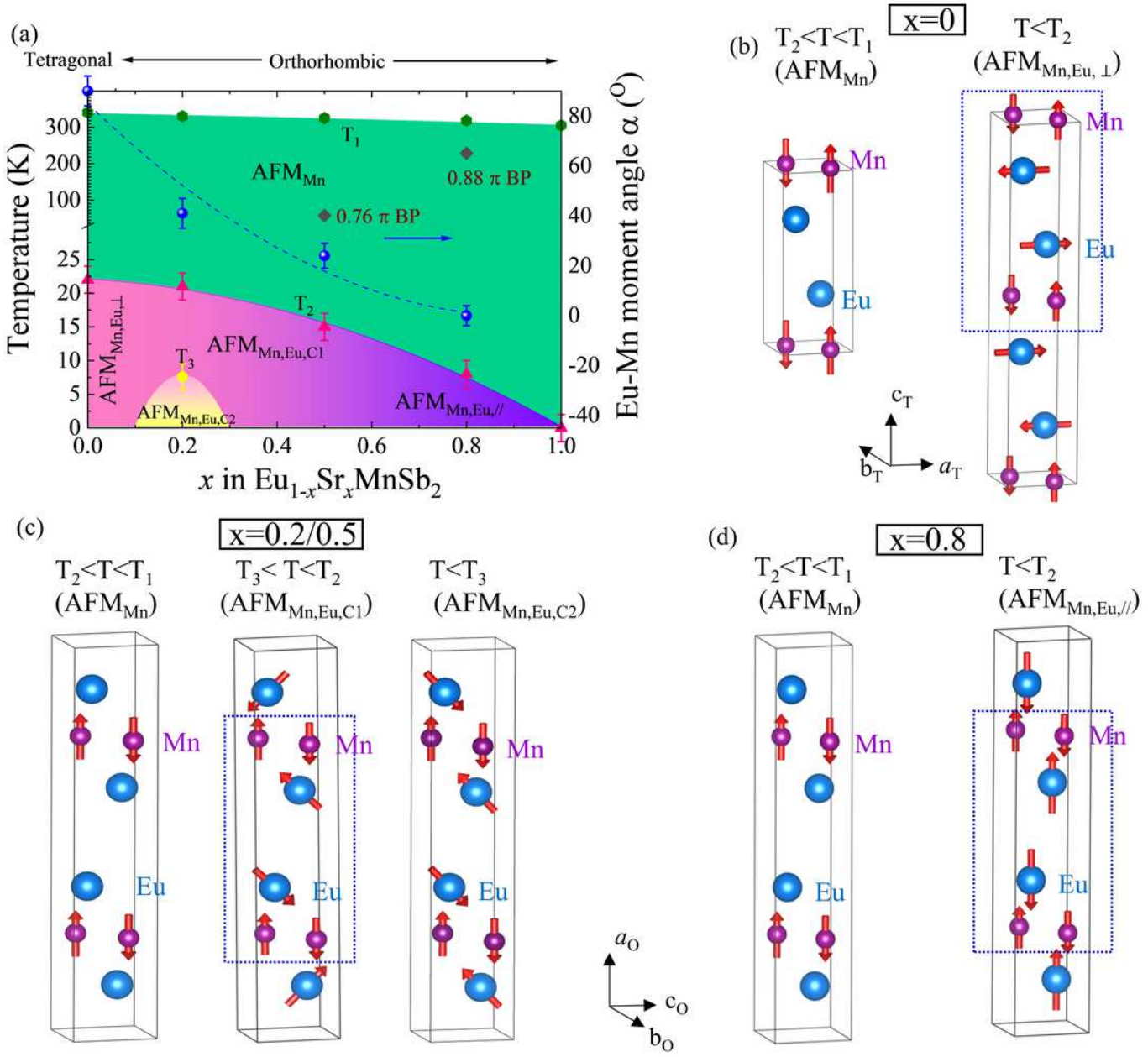

Figure 1

(color online) (a). Composition phase diagram of Eu1-xSrxMnSb2 on the structural and magnetic transitions, Eu-Mn moment angle α and nontrivial Berry phase (BH) extracted from the fits to ρin. T1, T2, and T3 label the magnetic transition temperatures. The distinct magnetic structures (AFMMn, AFMMn;Eu;?, AFMMn;Eu;C1, AFMMn;Eu;C2 and AFMMn;Eu;k) are displayed in Fig. 1(b-d). AFMMn;Eu;k and AFMMn;Eu;? indicate the parallel and perpendicular moments of Mn and Eu, respectively. AFMMn;Eu;C1 and AFMMn;Eu;C2 show the two distinct canted moments between Mn and Eu. The evolution of the violet color illustrates the gradual decrease of the Eu-Mn moment angles. A higher Eu

canting angle of (90o - α), i.e., a smaller α, is accompanied with the stronger quantum SdH oscillations. All the compounds exhibit metal-like transport properties as a function of temperature and they are also coupled to Eu order at T2 and T3. The non-trivial Berry phases indicative of Dirac semimetallic behaviors emerge with x ≥0.5. Magnetic structures determined from the fits to the neutron data for (b) x=0, (c) x=0.2 (all the panels) and 0.5 (only left and middle panels), and (d) x=0.8. The dashed rectangular shows the Mn-Eu-Eu-Mn block where the SR of Eu can be seen.

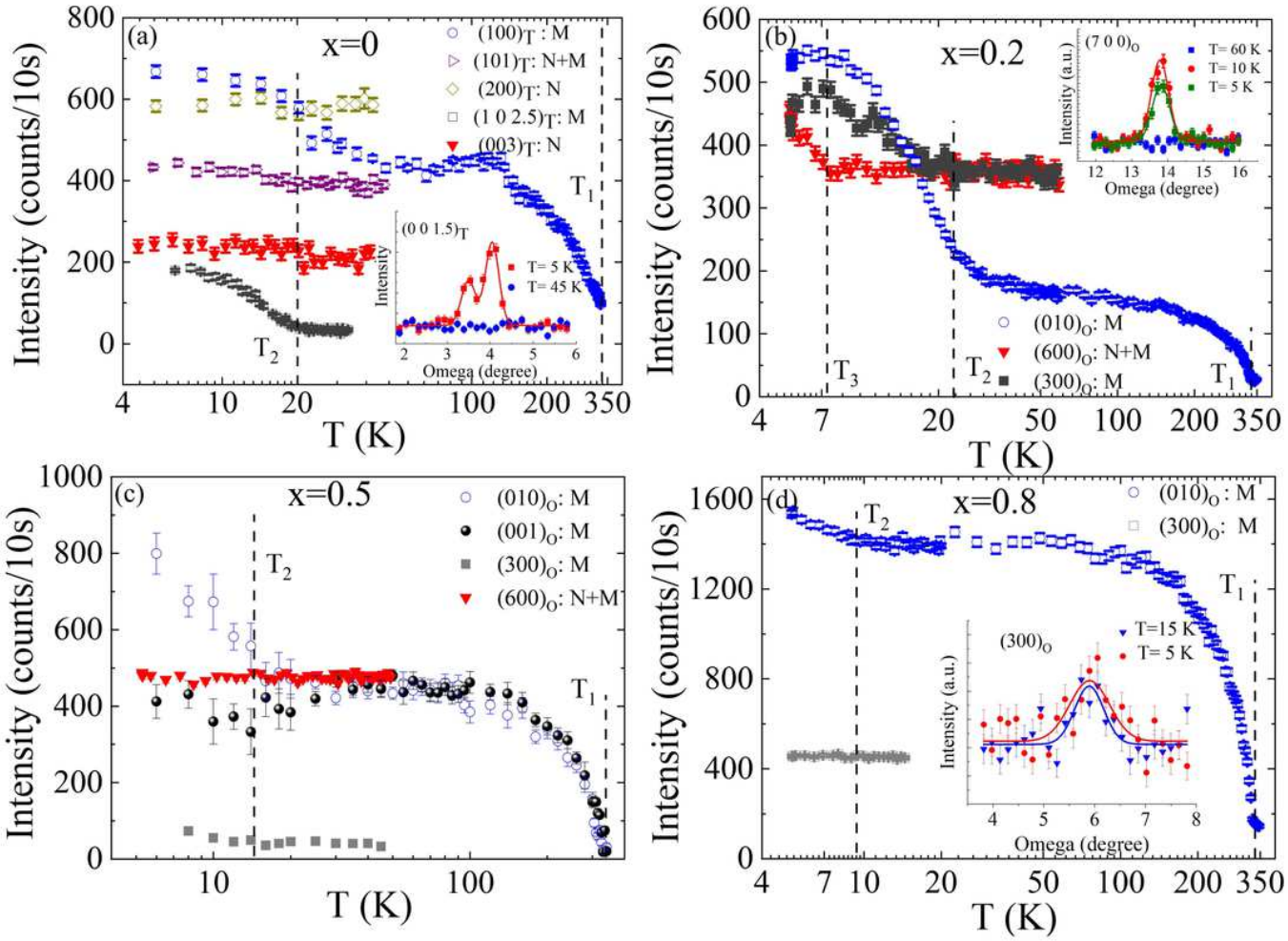

Figure 2

(color online) Temperature dependence of intensities at the representative nuclear and/or magnetic peak positions for (a) x=0, (b) x=0.2, (c) x=0.5, and (d) 0.8. The insets show the comparison of the nuclear/magnetic peaks at different temperatures. The 2nd weak peak with smaller omega in the rocking curves for x=0 is due to the presence of another tetragonal domain rather than orthorhombic domain in the crystal. The very weak (300) peak in (d) results from the ≥=2 contamination of neutrons. The vertical lines indicate the locations of the magnetic transition temperatures.

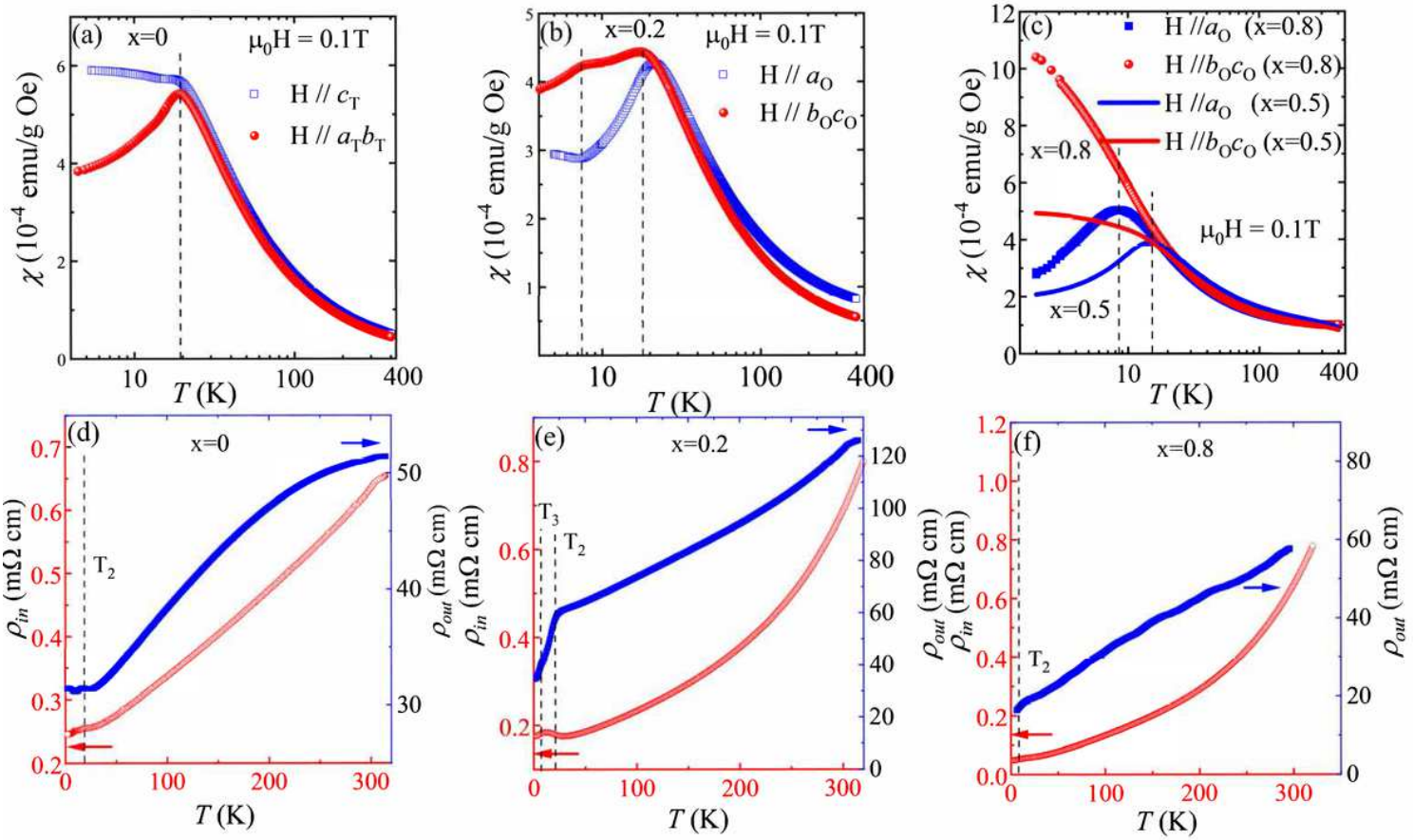

Figure 3

(color online) Temperature dependence of susceptibility for (a) x=0 with magnetic field of 0.1 T parallel to out-of-plane cT and in-plane aTbT directions, (b) x= 0.2, and (c) x=0.5 and 0.8, with field parallel to out-of-plane aO and in-plane bOcO directions. Temperature dependence of resistivity at zero magnetic field for out-of-plane resistivity ρout and in-plane resistivity ρin for (d) x=0, (e) x=0.2 and (f) x=0.8.

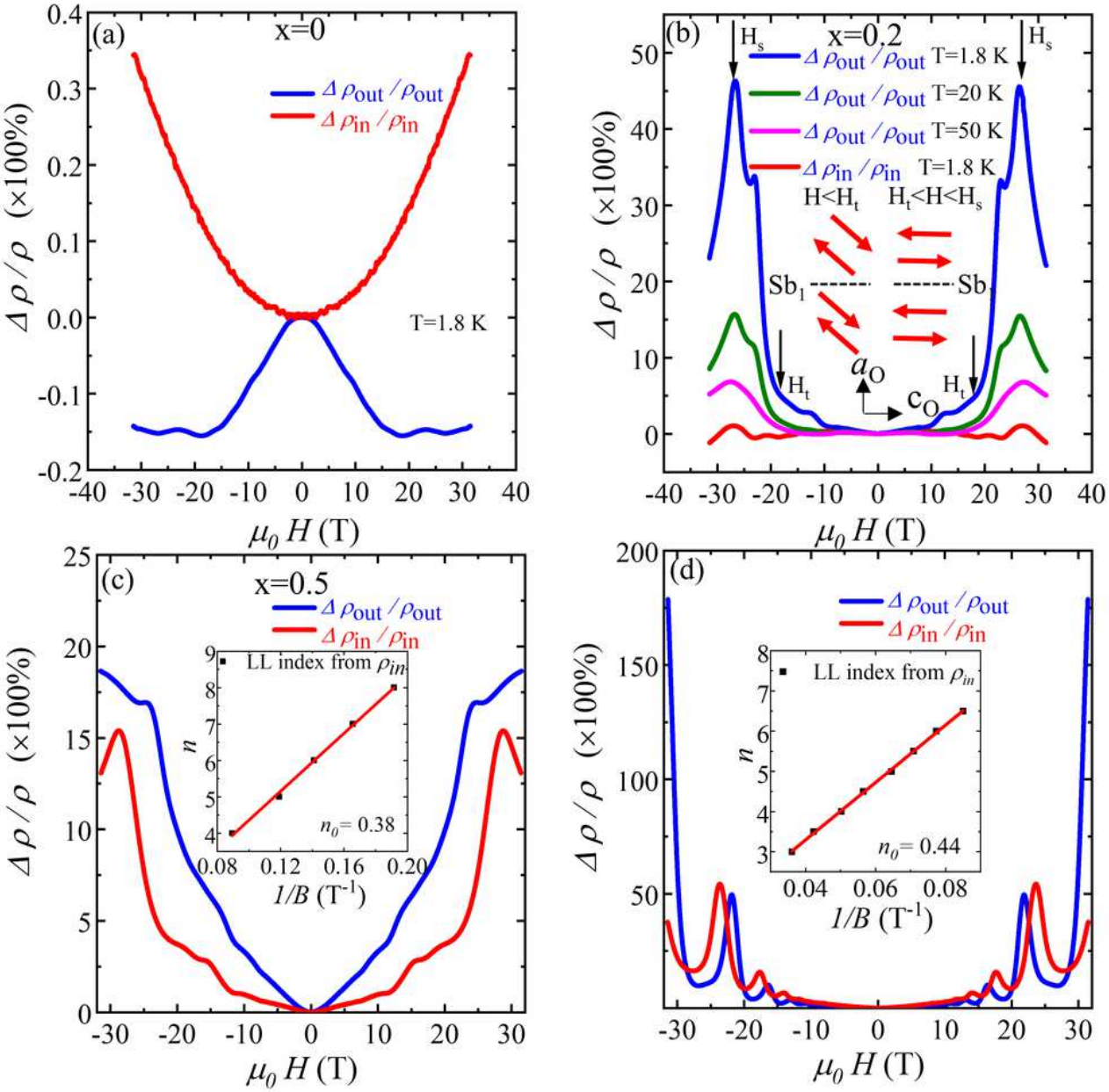

Figure 4

(color online) Field dependence of out-of-plane magnetoresistance Δρout=ρout and inplane magnetoresistance Δρin=ρin for (a) x=0, (b) x=0.2, (c) x=0.5, and (d) x=0.8. The inset of Fig. (b) shows the field-induced metamagnetic transition in Eu-sublattice, i.e., Eu spin ordering in and H < Hf and Hf < H < Hs. The inset of (c-d) shows the linear fit of the Landau level fan diagram based on the oscillatory resistivity ρin for x=0.5 and 0.8.

Supplementary Files

This is a list of supplementary files associated with this preprint. Click to download.

- EuSrMnSb2SMQZhangAll.pdf